DEVELOPMENT OF AN ARTIFICIAL COMPRESSIBILITY METHODOLOGY USING FLUX VECTOR SPLITTING

TH. PAPPOU AND S. TSANGARIS*

Laboratory of Aerodynamics, National Technical University of Athens, PO Box 64070, 15710 Zografou, Athens, Greece

SUMMARY

An implicit, upwind arithmetic scheme that is efficient for the solution of laminar, steady, incompressible, two-dimensional flow fields in a generalised co-ordinate system is presented in this paper. The developed algorithm is based on the extended flux-vector-splitting (FVS) method for solving incompressible flow fields. As in the case of compressible flows, the FVS method consists of the decomposition of the convective fluxes into positive and negative parts that transmit information from the upstream and downstream flow field respectively. The extension of this method to the solution of incompressible flows is achieved by the method of artificial compressibility, whereby an artificial time derivative of the pressure is added to the continuity equation. In this way the incompressible equations take on a hyperbolic character with pseudopressure waves propagating with finite speed. In such problems the 'information' inside the field is transmitted along its characteristic curves. In this sense, we can use upwind schemes to represent the finite volume scheme of the problem's governing equations. For the representation of the problem variables at the cell faces, upwind schemes up to third order of accuracy are used, while for the development of a time-iterative procedure a first-order-accurate Euler backward-time difference scheme is used and a second-order central differencing for the shear stresses is presented. The discretized Navier–Stokes equations are solved by an implicit unfactored method using Newton iterations and Gauss–Siedel relaxation. To validate the derived arithmetical results against experimental data and other numerical solutions, various laminar flows with known behaviour from the literature are examined. © 1997 by John Wiley & Sons, Ltd.

1. INTRODUCTION

Various time-dependent methods, both implicit and explicit, have been proposed during the last two decades for the solution of incompressible flow fields. For the development of implicit iterative procedures for incompressible flows the discretization of the Navier–Stokes equations requires particular consideration, since the time derivative of the density no longer appears. Hence the time-dependent implicit methods suitable for compressible flows cannot be applied without adaptation.

For time-iterative procedures one approach consists of solving the time-dependent momentum equations in connection with a Poisson equation for the pressure obtained by taking the divergence of the momentum equations and expressing the condition of the divergence-free velocity field; this is a pressure correction method. The above method of solving Poisson's equation for the pressure was developed first by Harlow and Welch.[1]

---

* Correspondence to: S. Tsangaris, Laboratory of Aerodynamics, National Technical University of Athens, PO Box 64070, 15710 Zografou, Athens, Greece.

An arithmetic structure similar to the compressible equations can be recovered by adding an artificial compressibility term in the form of the time derivative of the pressure to the continuity equation. This is the pseudocompressibility method introduced initially by Chorin[2] and Steger and Kutler[3] and developed for the solution of steady, unsteady and 3D flow fields by Peyret and Taylor,[4] Chang and Kwak,[5] Choi and Merkle,[6] Rizzi and Erikson,[7] Kwak et al.,[8] Merkle and Athavale,[9] Soh and Goodrich[10] and others.

The incompressible equations after the addition of the pseudocompressibility term take on a hyperbolic character with pseudopressure waves propagating with finite speed. In such problems 'the information' inside the flow field is transmitted along its characteristic curves. In this sense we can relate the sign of eigenvalues to the upwind representation of the flow variables at the cell faces. The upwinding of the inviscid fluxes gives more freedom in devising implicit algorithms[3,11] since it loads up the diagonals of the implicit factors. Upwind differencing[12,13] also alleviates the necessity to add and tune the numerical dissipation for numerical stability and accuracy as in the schemes with central differencing that belong to the family of Beam–Warming schemes.[14]

The upwind scheme of the hyperbolic problem in this paper is based on the extended (by the method of pseudocompressibility) flux-vector-splitting (FVS) method. FVS is a shock-capturing upwind method that is well known for solving compressible high-speed (transonic and hypersonic) flows. Two of the best known FVS methods are those of Steger and Warming[15] and van Leer.[16]

Steger and Warming's FVS method is based on the splitting of the flux vectors into positive and negative parts. The positive part carries upstream 'information' and relates to the positive eigenvalues of the problem. The negative part carries downstream 'information' and relates to the negative eigenvalues of the problem. In hyperbolic problems (compressible flows) at each directory separately the eigenvalues give characteristic curves along which the information is transmitted inside the field. For the above splitting the homogeneous property of the Euler equation is used. This property is valid because of the existence of an equation of state for gases.

The FVS method of van Leer constructs the fluxes as a function of the local Mach number.

Here, we extend the FVS method of Steger and Warming for solving incompressible flow fields implicitly, based on the implicit scheme of References 17–19. In such flow fields the splitting of the convective flux vectors has to change sense because of their non-homogeneous property. This is a very important element of the present study.

The values of the flux vectors at the cell faces are approached by upwind schemes up to third order of accuracy, such as the MUSCL (monotone upstream centred for conservation law) scheme[3] and hybrid upwind extrapolation.[19]

The unfactored discretized Navier–Stokes equations are solved by an implicit first-order-accurate (in time) scheme using a Gauss–Seidel relaxation technique. This is also an important new element of the present study, because in this way the errors that coexist with an implicit method of approximate factorization are avoided.

The governing equations of the problem are presented in Section 2. In Section 3 the new flux-vector-splitting method, the finite volume formulation and the upwind schemes used are developed. In Section 4 the described numerical method is applied for the calculation of various flow fields in order to validate the present results against experimental data and numerical results from other arithmetic schemes.

2. GOVERNING EQUATIONS

The dimensionless Navier–Stokes equations for the representation of 2D incompressible flow fields after the addition of the pseudocompressibility term to the continuity equation, in conservative form

in a Cartesian system of co-ordinates (x, z), are

$$\frac{\partial q}{\partial t} + \frac{\partial e}{\partial x} + \frac{\partial g}{\partial z} = \frac{1}{Re}\left(\frac{\partial r}{\partial x} + \frac{\partial s}{\partial z}\right), \tag{1}$$

where Re is the Reynolds number for the examined flow field, $q = (p/\beta, u, w)^{\mathrm{T}}$ is the conservative unknown solution vector (p is the pressure, β is the pseudocompressibility parameter and u and w are the velocity components) and e, g and r, s are the convective and diffusive flux vectors respectively at the plane (x, z):

$$\begin{aligned} e &= (u, u^2 + p, uw)^{\mathrm{T}}, & g &= (w, uw, w^2 + p)^{\mathrm{T}}, \\ r &= (0, \tau_{xx}, \tau_{xz})^{\mathrm{T}}, & s &= (0, \tau_{zx}, \tau_{zz})^{\mathrm{T}}. \end{aligned} \tag{2}$$

The shear stresses are expressed as

$$\tau_{xx} = -\tfrac{2}{3}(-2u_x + w_z), \qquad \tau_{xz} = \tau_{zx} = (u_z + w_x), \qquad \tau_{zz} = -\tfrac{2}{3}(u_x - 2w_z). \tag{3}$$

The governing equations after the transformation to a generalized system of co-ordinates (ξ, ζ) take the form

$$\frac{\partial Q}{\partial t} + \frac{\partial E}{\partial \xi} + \frac{\partial G}{\partial \zeta} = \frac{1}{Re}\left(\frac{\partial R}{\partial \xi} + \frac{\partial S}{\partial \zeta}\right), \tag{4}$$

with E, G and S, R the transformed inviscid and viscous flux vectors respectively:

$$\begin{aligned} E &= J(e\xi_x + g\xi_z), & G &= J(e\zeta_x + g\zeta_z), \\ R &= J(r\xi_x + s\xi_z), & S &= J(r\zeta_x + s\zeta_z). \end{aligned} \tag{5}$$

Thus the inviscid flux vectors are

$$E = (U, uU + p\xi_x, wU + p\xi_z)^{\mathrm{T}}, \qquad G = (W, uW + p\zeta_x, wW + p\zeta_z)^{\mathrm{T}}, \tag{6}$$

where $U = u\xi_x + w\xi_z$ and $W = u\zeta_x + w\zeta_z$ are the contravariant components of the velocity vector at the transformed plane. $J = x_\xi z_\zeta - x_\zeta z_\xi$ is the Jacobian of the transformation from Cartesian co-ordinates (x, z) to generalized co-ordinates (ξ, ζ).

The unsteady term added to the continuity equation is the quantity $(1/\beta)\partial p/\partial t$. The addition of the pseudocompressibility term causes the unsteady terms of the momentum equations to lose their physical meaning, which is only recovered at steady state, where the divergence-free condition of the continuity equation is satisfied. Thus the time derivative of the conservative solution vector of (1) or (4) acts as an auxiliary term for the construction of a hyperbolic system of equations. As a result, some of the available implicit arithmetic methods can be adapted for the prediction of a steady state solution; here the adaptation of the FVS method is presented. In this way the coupling of the fluid pressure with the velocity vector of the flow field, which is the primary problem in the solution of incompressible flow fields, is achieved.

3. IMPLICIT SCHEME AND FLUX-VECTOR-SPLITTING METHOD

3.1. Time integration and flux-splitting method

Flux-splitting methods are based on the splitting of the convective vectors, so in this section the finite volume scheme for the Euler equations is considered:

$$\frac{\partial Q}{\partial t} + \frac{\partial E}{\partial \xi} + \frac{\partial G}{\partial \zeta} = 0. \tag{7}$$

The first-order (in time) discretized implicit scheme for the Euler equations has the form:

$$\frac{Q^{n+1} - Q^n}{\Delta t} + \frac{\partial E^{n+1}}{\partial \xi} + \frac{\partial G^{n+1}}{\partial \zeta} = 0. \tag{8}$$

A Newton iterative method can be constructed for the prediction of U^{n+1} by linearizing the fluxes in (8) about the known time level n:

$$E^{n+1} = E^n + A^n \Delta Q, \tag{9a}$$

$$G^{n+1} = G^n + C^n \Delta Q, \tag{9b}$$

where $A = \partial E / \partial Q$ and $C = \partial G / \partial Q$ are the Jacobian matrices of the flux vectors E and G respectively and $\Delta Q = Q^{n+1} - Q^n$ is the correction of the conservative variables between two successive time levels of the iterative procedure. The above linearizations yield equation (8) in the form

$$\frac{Q^{n+1} - Q^n}{\Delta t} + (A^n \Delta Q)_\xi + (C^n \Delta Q)_\zeta = -(E_\xi + G_\zeta)^n. \tag{10}$$

The flux-vector-splitting method consists of the decomposition of the convective flux vectors into two parts in accordance with the sign of the eigenvalues:

$$E = E^+ + E^-, \tag{11a}$$

$$G = G^+ + G^-. \tag{11b}$$

Therefore the upwind representation of the fluxes at the cell faces of the cell-centred collocated grid, which is required for the discrete representation of the flux derivatives on the RHS of (10), is achieved. This splitting gives the direction of the upwinding when the discrete representation of the flux vectors E_ξ and G_ζ is obtained by the differences in the values of the fluxes E and G at the cell faces.

This approximation for the fluxes E_ξ and G_ζ for the FVS method with the use of upwind differencing is accomplished in the case of compressible flows, where the fluxes are homogeneous functions of the primitive variable vector Q. The homogeneous property is valid because of the existence of an equation of state in the case of a compressible fluid.

In the case of incompressible flow as examined in this paper, the homogeneous property for the flux vector is not valid. Thus for the split representation of the flux vectors E_ξ and G_ζ the following interpretation is used:

$$\frac{\partial E}{\partial \xi} = \frac{\partial E}{\partial Q}\frac{\partial Q}{\partial \xi} = A \frac{\partial Q}{\partial \xi}, \tag{12a}$$

$$\frac{\partial G}{\partial \zeta} = \frac{\partial G}{\partial Q}\frac{\partial Q}{\partial \zeta} = C \frac{\partial Q}{\partial \zeta}. \tag{12b}$$

The discretization of the flux vectors here requires the upwind representation of the vector variables Q at the cell faces in accordance with the sign of the eigenvalues of the Jacobian matrices A and C. The splitting of the fuses is achieved by the splitting of the Jacobian matrices A and C into a

positive and a negative part related to the positive and negative eigenvalues respectively, as in the case of compressible flows. Specifically the splitting of the present method takes the form

$$\frac{\partial E}{\partial \xi} = A^+ \frac{\partial Q^+}{\partial \xi} + A^- \frac{\partial Q^-}{\partial \xi} = (T\Lambda^+ T^{-1})\frac{\partial Q^+}{\partial \xi} + (T\Lambda^- T^{-1})\frac{\partial Q^-}{\partial \xi}, \tag{13a}$$

$$\frac{\partial G}{\partial \zeta} = C^+ \frac{\partial Q^+}{\partial \zeta} + C^- \frac{\partial Q^-}{\partial \zeta} = (NL^+ N^{-1})\frac{\partial Q^+}{\partial \zeta} + (NL^- N^{-1})\frac{\partial Q^-}{\partial \zeta}, \tag{13b}$$

where Λ and L are the diagonal matrices of the eigenvalues of the Jacobian matrices A and C respectively. These matrices are decomposed into a positive (Λ^+, L^+) and a negative (Λ^-, L^-) part containing the positive and negative eigenvalues respectively. Specifically, the values of the above quantities for the Jacobian A are $\Lambda = \mathrm{diag}[\lambda_0, \lambda_1, \lambda_2]$, $\Lambda = \Lambda^+ + \Lambda^-$, with $\Lambda^+ = \mathrm{diag}[\lambda_0^+, \lambda_1^+, \lambda_2^+]$ and $\Lambda^- = \mathrm{diag}[\lambda_0^-, \lambda_1^-, \lambda_2^-]$, where $\lambda_i^\pm = (\lambda_i^\pm \pm |\lambda_i^\pm|)/2$, $i = 0, 1, 2$, $\lambda_0 = u\xi_x + w\xi_z = U$, $\lambda_1 = \lambda_0 + \sqrt{[\lambda_0^2 + \beta(\xi_x^2 + \xi_z^2)]}$ and $\lambda_2 = \lambda_0 - \sqrt{[\lambda_0^2 + \beta(\xi_x^2 + \xi_z^2)]}$, and the matrices T and T^{-1} are the left and right eigenvector matrices respectively. The corresponding values for the Jacobian C are $L = [\lambda_0, \lambda_1, \lambda_2]$, $L = L^+ + L^-$, with $L^+ = \mathrm{diag}[\lambda_0^+, \lambda_1^+, \lambda_2^+]$ and $L^- = \mathrm{diag}[\lambda_0^-, \lambda_1^-, \lambda_2^-]$, where $\lambda_i^\pm = (\lambda_i^\pm \pm |\lambda_i^\pm|)/2$, $i = 0, 1, 2$, $\lambda_0 = u\zeta_x + w\zeta_z = W$, $\lambda_1 = \lambda_0 + \sqrt{[\lambda_0^2 + \beta(\zeta_x^2 + \zeta_z^2)]}$ and $\lambda_2 = \lambda_0 - \sqrt{[\lambda_0^2 + \beta(\zeta_x^2 + \zeta_z^2)]}$, and the matrices N and N^{-1} are the left and right eigenvector matrices respectively.

The plus $(+)$ sign in (13) indicates the Jacobians A and C corresponding to the positive eigenvalues and dictates a backward upwinding for the quantities $\partial Q^+/\partial \xi$ and $\partial Q^+/\partial \zeta$, while the minus $(-)$ sign denotes the 'negative' matrices A and C and a forward upwinding for the quantities $\partial Q^-/\partial \xi$ and $\partial Q^-/\partial \zeta$.

The upwind discrete from of the derivatives of the vector variables can be considered in the following two ways.

(a) One can make the assumption

$$\left(\frac{\partial Q}{\partial \xi}\right)^+_{i,k} = Q^+_{i+1/2,k} - Q^+_{i-1/2,k}, \qquad \left(\frac{\partial Q}{\partial \xi}\right)^-_{i,k} = Q^-_{i+1/2,k} - Q^-_{i-1/2,k}, \tag{14a}$$

$$\left(\frac{\partial Q}{\partial \zeta}\right)^+_{i,k} = Q^+_{i,k+1/2} - Q^+_{i,k-1/2}, \qquad \left(\frac{\partial Q}{\partial \zeta}\right)^-_{i,k} = Q^-_{i,k+1/2} - Q^-_{i,k-1/2}. \tag{14b}$$

In this way the upwind representation of the vector variables at the cell faces is required and it is obtained from the sign of the eigenvalues at the centre of the current finite control volume.

(b) One can calculate the derivatives $\partial Q/\partial \xi$ and $\partial Q/\partial \zeta$ at the cell faces with central differencing of the values of the vector variables at the cell centres:

$$(Q_\xi)_{i+1/2,k} = Q_{i+1,k} - Q_{i,k}, \qquad (Q_\xi)_{i-1/2,k} = Q_{i,k} - Q_{i-1,k}, \tag{15a}$$

$$(Q_\zeta)_{i,k+1/2} = Q_{i,k+1} - Q_{i,k}, \qquad (Q_\zeta)_{i,k-1/2} = Q_{i,k} - Q_{i,k-1}. \tag{15b}$$

One consequently expresses with upwind representation the values of the derivatives of the vector variables at the centre of the control volume in accordance with the splitting of the Jacobian matrix A, thus increasing the order of accuracy of the arithmetic scheme used.

For both splittings the values of the Jacobian matrix A are calculated at the centre of the cell and in accordance with these splitting is obtained. Calculations have been made with both the above schemes for various test cases.

3.2. Unfactored implicit relaxation solution of Navier–Stokes equations

Time integration of the implicit unfactored equations is performed with a relaxation Gauss–Seidel method that allows high CFL numbers. The implicit algorithm is first-order-accurate in time.

The unfactored equations are solved by a Newton method constructing a sequence of approximations q^v such that $\lim_{v>1} q^v \to Q^{n+1}$, where v is the subiteration state. A Newton form is obtained with the linearization of (8), which has been described in Section 3.1, around the known subiteration state v as follows:

$$J\frac{\Delta q^{v+1}}{\Delta t} + (A_{inv}^v \Delta q^{v+1})_\xi + (C_{inv}^v \Delta q^{v+1})_\zeta + (A_{vis}^v \Delta q^{v+1})_\xi + (C_{vis}^v \Delta q^{v+1})_\zeta = J\frac{Q^n - q^v}{\Delta t} - \text{RHS}, \quad (16)$$

with

$$\text{RHS} = \left(E_\xi + G_\zeta - \frac{1}{Re}(R_\xi + S_\zeta)\right)^n,$$

where q^v and q^{v+1} are the solution vectors at the subiteration states v and $v+1$ respectively. A_{inv}, C_{inv} and A_{vis}, C_{vis} are the Jacobian matrices of the inviscid (E, G) and viscous (R, S) fluxes respectively. The Jacobian matrices of the viscous terms, A_{vis} and C_{vis}, have been calculated by taking into account the fact that the viscous fluxes are functions of the velocity components and of the spatial derivatives of the velocity components as well, in order to ensure the second-order accuracy of the present scheme.

The terms $(A_{inv}^v \Delta q^{v+1})_\xi$, $(C_{inv}^v \Delta q^{v+1})_\zeta$, $(A_{vis}^v \Delta q^{v+1})_\xi$ and $(C_{vis}^v \Delta q^{v+1})_\zeta$ or the LHS of (16) are discretized at (i, k) with a scheme of up to second-order accuracy in space. For example, for the quantity $(A_{inv}^v \Delta q)_\xi + (A_{vis}^v \Delta q)_\xi$ at the cell (i, k) we apply the scheme:[20]

$$(A_{inv}^v \Delta q)_\xi + (A_{vis}^v \Delta q)_\xi = (A_{inv}^v \Delta q)_{i+1/2} - (A_{inv}^v \Delta q)_{i-1/2} + (A_{vis})_i(\Delta q_{i+1} - 2\Delta q_i + \Delta q_{i-1}). \quad (17)$$

The above inviscid fluxes of the LHS of (16) are split as

$$(A_{inv}^v \Delta q)_{i+1/2} = (T\Lambda^+ T^-)_{i+1/2}\Delta q_{i+1/2}^+ + (T\Lambda^- T^{-1})_{i+1/2}\Delta q_{i+1/2}^-, \quad (18a)$$

$$(A_{inv}^v \Delta q)_{i-1/2} = (T\Lambda^+ T^-)_{i-1/2}\Delta q_{i-1/2}^+ + (T\Lambda^- T^{-1})_{i-1/2}\Delta q_{i-1/2}^-, \quad (18b)$$

with Δq extrapolated consistently to the right-hand side:

$$\Delta q_{i+1/2}^+ = \beta\Delta q_i + (1 - \beta)(1{\cdot}5\Delta q_i - 0{\cdot}5\Delta q_{i-1}), \quad (19a)$$

$$\Delta q_{i-1/2}^- = \beta\Delta q_i + (1 - \beta)(1{\cdot}5\Delta q_i - 0{\cdot}5\Delta q_{i+1}), \quad (19b)$$

$$\Delta q_{i+1,2}^- = \Delta q_{i+1}, \quad (19c)$$

$$\Delta q_{i-1/2}^+ = \Delta q_{i-1}. \quad (19d)$$

The matrices T, Λ and T^{-1} are calculated at the cell faces from arithmetic means of the conservative variables. For the finite volume face $(i + \frac{1}{2}, k)$, Δq is extrapolated up to second order for positive eigenvalues depending on the sensor β. The parameter β is taken as a function sensing the non-monotonic distribution of pressure in the flow field in order to reduce the order of extrapolation down to first order to guarantee monotonic behaviour of the flow field in regions with increased pressure gradients.

After the discrete representation of the LHS and RHS quantities a point Gauss–Seidel technique is used for the solution of the system of algebraic equations for the correction vector variable $\Delta q(i, k)$.

In accordance with the present techniques, at the LHS there remain only the terms that contribute to the diagonal term (i, k) as coefficients of the unknown vector $\Delta q_{i,k}$. One term of this coefficient is the quantity $J/\Delta t$ that strengthens diagonal dominance and therefore stability. The resultant system is a 3×3 system of algebraic equations.

A Gauss–Seidel relaxation technique using six subiteration states is applied on the LHS of (16), while the RHS is held constant at each of the two Newton subiterations (v) that are accomplished for the solution of (16). The fluxes at the RHS from the previous time step are multiplied by an overrelaxation factor ω that compensates errors of different spatial order of accuracy on the RHS and LHS and accelerates the convergence to the steady state; this is permissible because the RHS approaches zero as the steady state solution is reached.

3.3. Upwind schemes

For the calculation of the plus ($+$) and minus ($-$) states of either the conservative variables Q at the cell faces or the derivatives of the conservative variables at the centre of each cell we use extrapolation formulae of up to third-order accuracy. Here it is recalled that for the numerical representation of the computational domain a cell-centred collocated rectilinear grid is used.

The schemes used for the upwind representation are as follows.

Hybrid upwind extrapolation. In the literature, FVS methods for compressible flows have been developed using this class of upwind schemes with third and fourth orders of accuracy. Here we use the same formulations for up to third-order-accurate approaches.

(a) First order (classic upwinding):

$$(Q^1_{i+1/2,k})^+ = Q_{i,k}, \qquad (Q^1_{i+1/2,k})^- = Q_{i+1,k}. \tag{20}$$

(b) Second order:

$$(Q^2_{i+1/2,k})^+ = \tfrac{1}{2}(3Q_{i,k} - Q_{i-1,k}), \qquad (Q^2_{i+1/2,k})^- = \tfrac{1}{2}(3Q_{i+1,k} - Q_{i+2,k}). \tag{21}$$

(c) Third order:

$$(Q^3_{i+1/2,k})^+ = \tfrac{1}{6}(5Q_{i,k} - Q_{i-1,k} + 2Q_{i+1,k}), \tag{22}$$

$$(Q^3_{i+1/2,k})^- = \tfrac{1}{6}(5Q_{i+1,k} - Q_{i+2,k} + 2Q_{i,k}). \tag{23}$$

MUSCL scheme. In the case of compressible flows this is one of the most used extrapolations. Here it is used for incompressible flows too. It is the following three-point scheme:

$$
\begin{aligned}
Q^+_{i+1/2,k} &= Q_{i,k} + \frac{g_{i,k}}{4}[(1 - kg_{i,k})\nabla + (1 + kg_{i,k})\Delta]Q_{i,k}, \\
Q^-_{i+1/2,k} &= Q_{i+1,k} - \frac{g_{i+1,k}}{4}[(1 + kg_{i+1,k})\nabla + (1 - kg_{i+1,k})\Delta]Q_{i+1,k},
\end{aligned}
\tag{24}
$$

with $\Delta Q_{i,k} = Q_{i+1,k} - Q_{i,k}$ and $\nabla Q_{i,k} = Q_{i,k} - Q_{i-1,k}$. The spatial accuracy depends on the parameter k. For instance, $k = -1$ produces fully upwinded, $k = 0$ symmetric, $k = \tfrac{1}{3}$ third-order biased and $k = 1$ centred schemes. The limiter g is the van Albada sensor[21]

$$g_{i,k} = \frac{1}{2}\frac{\nabla Q_{i,k}\Delta Q_{i,k}}{(\nabla Q_{i,k})^2 + (\Delta Q_{i,k})^2 + \varepsilon}, \tag{25}$$

where ε is a small number. The role of the limiter in compressible flows is to reduce the order of accuracy in those regions where strong discontinuities of the flow are observed. Such regions are in the vicinity of shock waves.

3.4. Boundary conditions

For the imposition of boundary conditions on the flow field, pseudocells are set all around the computational domain. The imposed values of the problem variables at these cells are such that their interpolation with values from interior cells gives the prescribed conditions at the boundaries of the flow field.

For the case of an inviscid fluid the free slip condition is imposed at the solid and freestream boundaries. For viscous flow at the no-slip surfaces the velocity vector is specified to be zero and the normal to the surface pressure gradient is set to zero in accordance with boundary layer theory. Furthermore, boundary conditions are prescribed on ΔQ in phantom cell rows. At the boundaries where the variables Q are prescribed, the corresponding vector ΔQ is set equal to zero, while at the boundaries where Q is calculated by extrapolation, the quantity ΔQ is also calculated by extrapolation of the same order of accuracy as for Q.

For internal flows at the outflow boundary a constant static pressure is imposed and fully developed flow is assumed for the prediction of the velocity components.

4. VALIDATION OF NUMERICAL METHOD AND RESULTS

4.1. Flow over a backward-facing step

4.1.1. Flow over a backward-facing step for Re = 389. In this case the flow over a backward-facing step for $Re = 389$ is examined and the computational results are compared with the corresponding experimental data.[22] The geometry of the computational domain is shown in Figure 1. The reference quantities used for the calculation of the Reynolds number are the mean velocity of the fluid at the inlet, which is equal to two-thirds of the measured maximum velocity, as U_{ref} and the hydraulic diameter of the inlet (small) channel, which is equivalent to twice its height ($D = 2h$), as L_{ref}.

At the inlet cross-sectional area a parabolic profile was imposed for the axial dimensionless velocity $u = 24z(0.5 - z)$ for $0 \leqslant z \leqslant 0.5$ and the vertical velocity component w was set equal to zero. For the corresponding pressure we assumed zero pressure gradient in the x-direction. On the solid walls of the above geometry the no-slip condition was imposed for the velocity components and zero normal pressure gradient was taken for the computation of pressure. At the exit, fully developed flow was assumed. This fact dictates zero gradient in the x-direction for the velocity components and
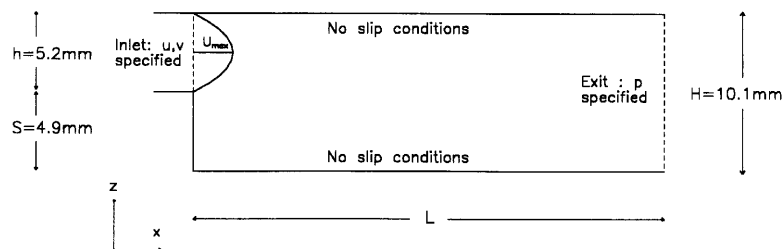

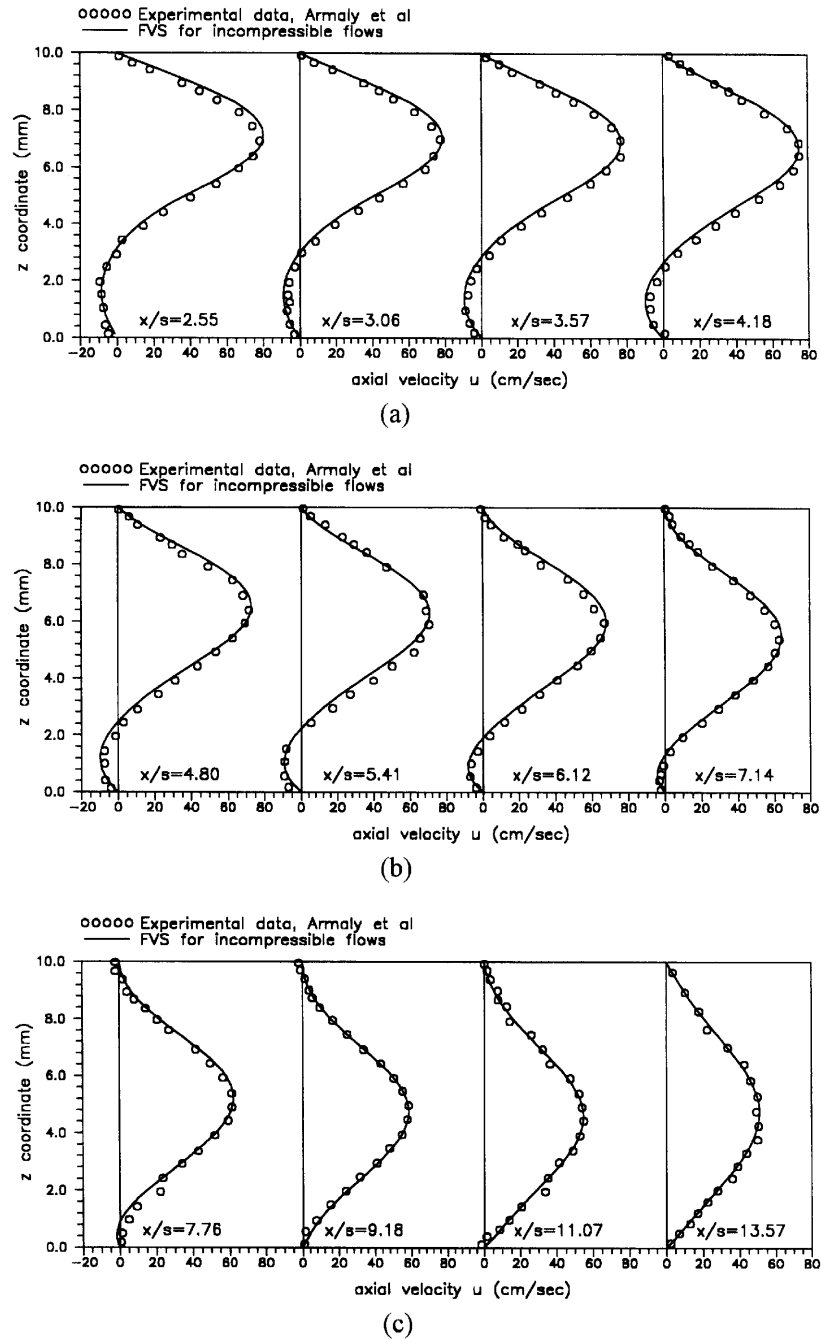Figure 1. Dimensional schematic representation of backward-facing step geometry

Figure 2. Comparisons of axial velocity profiles of u-velocity component at various stations along channel with corresponding experimental data of Armaly et al.:[22] (a) $x/s = 2\cdot55$, $3\cdot06$, $3\cdot57$ and $4\cdot18$; (b) $x/s = 4\cdot80$, $5\cdot41$, $6\cdot12$ and $7\cdot14$; (c) $x/s = 7\cdot76$, $9\cdot18$, $11\cdot07$ and $13\cdot57$
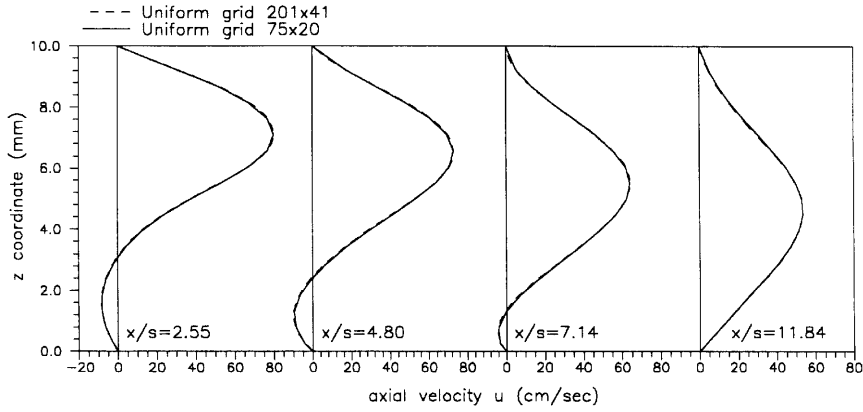
Figure 3. Horizontal velocity profiles along channel for two different grids: $x/s = 2.55$, 4.80, 7.14 and 11.84

constant pressure (equal to zero) at the exit cross-sectional area. In order to warrant the condition of fully developed flow, the total dimensionless length of the channel was taken as $L = 15$.

The resultant profiles of the axial velocity component at various stations along the channel are in good agreement with the corresponding available experimental data,[22] as can be seen in Figures 2(a)–(c).

Two different grids (with increasing number of nodes) we used to ensure the grid size independence of the present results (Figure 3).

An investigation of the influence of the limiter on the MUSCL scheme is also attempted. The introduction of the van Albada limiter for the reduction of the accuracy of the upwind scheme in the vicinity of discontinuities seems not to influence the accuracy of the results for the same grid as above (75×20) (Figure 4), but it has the valuable capability of a marked reduction of the iterations for convergence of the flow field. This impressive reduction is evident in Figures 5(a)–5(c), where the convergence histories of the flow field primitive variables are presented.
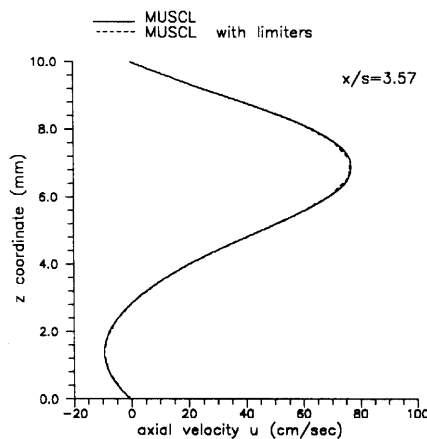
Figure 4. Represenative axial velocity profile for comparison of MUSCL schemes with and without addition of limiters: $x/s = 3.57$

(a)

(b)

(c)
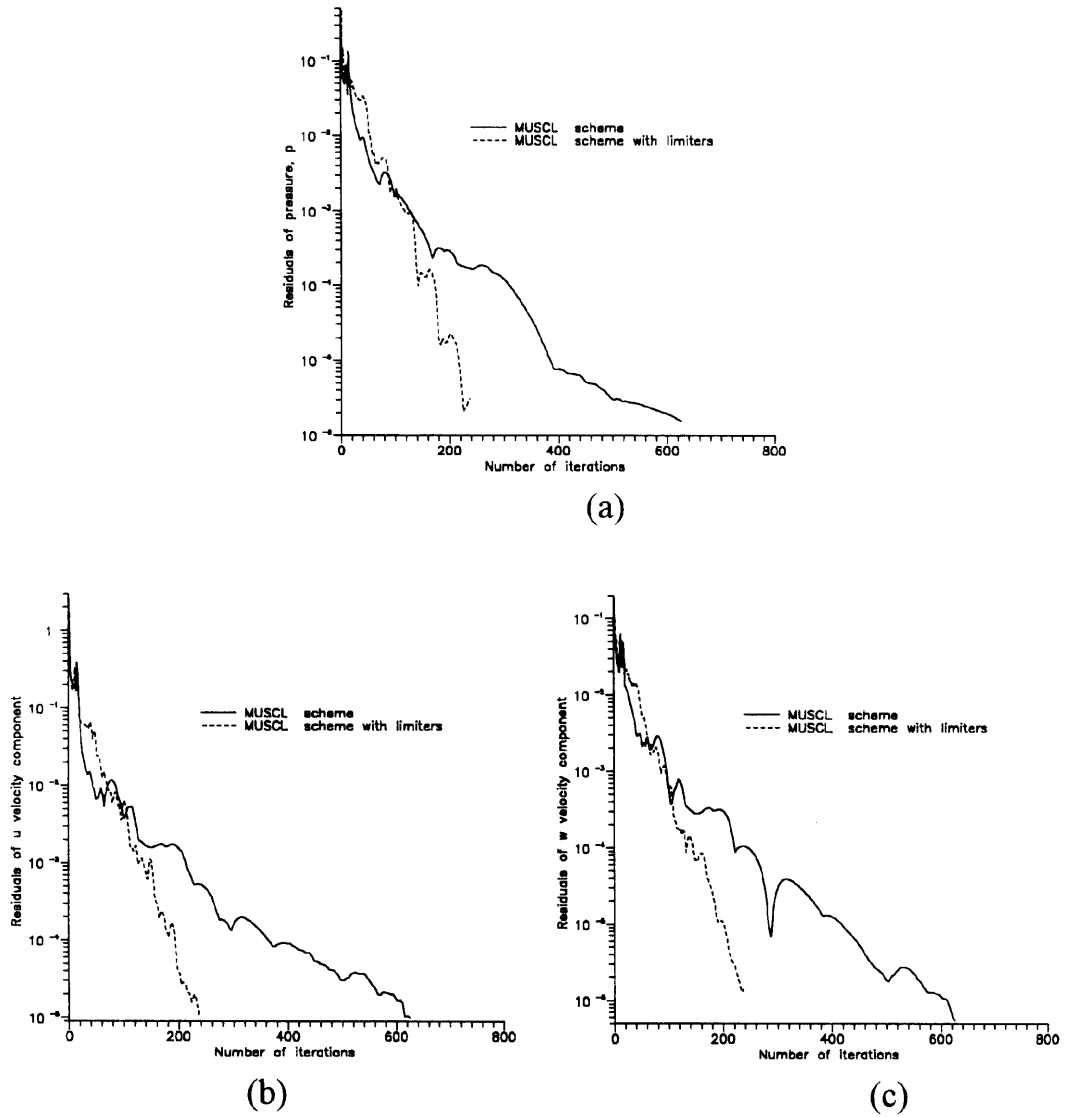
Figure 5. Convergence histories of primitive flow variables of MUSCL schemes with and without addition of limiters: (a) pressure; (b) u-velocity component; (c) w-velocity component
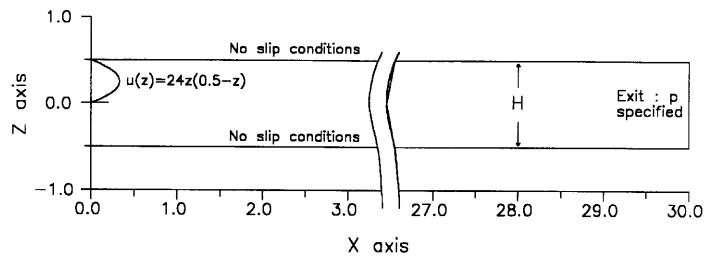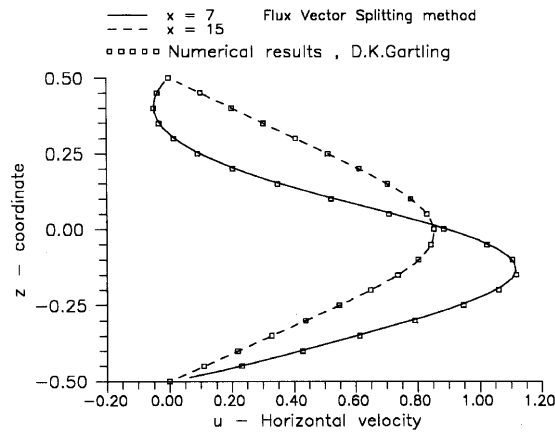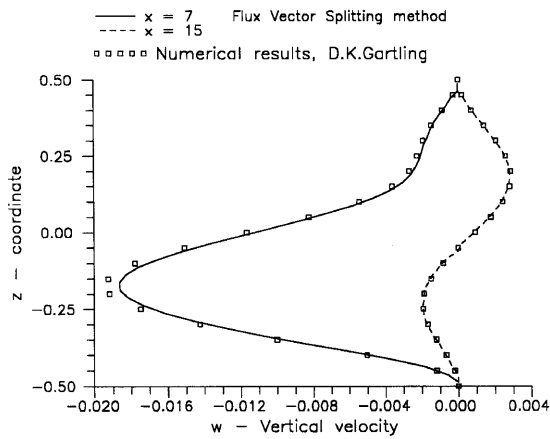

Figure 6(a). Dimensionless backward-facing step geometry
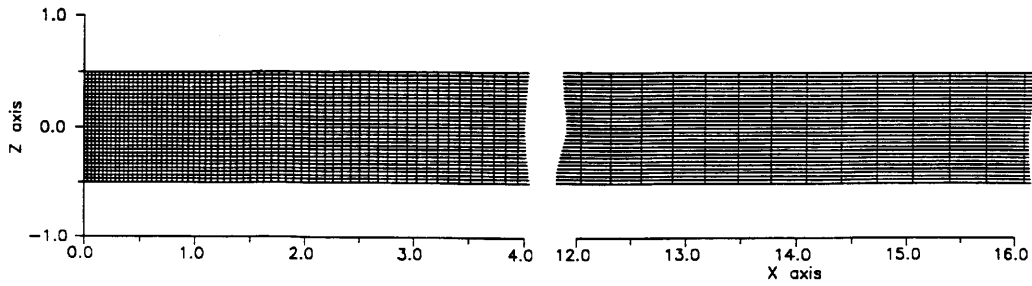
Figure 6(b). Non-uniform 150 × 31 grid for discrete representation of computational domain

(a)

(b)

Figure 7. Comparison of (a) horizontal and (b) vertical velocity profiles at sections $x = 7$ and 15 with corresponding results of Gartling[23]

4.1.2. Flow over a backward-facing step for Re = 800. In this flow field the important element is the precise prediction of the two recirculation zones that are developed downstream of the backward-facing step for $Re = 800$. This prediction is essential in the case of incompressible flows because of the fact that the existence of regions with high gradients of the flow field variables is closely related to regions where the velocity vector changes its direction. The geometrical data of the present computational domain are presented in Figure 6(a). *Re* was calculated with the following reference quantities. As U_{ref} the average inflow velocity was set and as L_{ref} the height H of the channel was set. The inlet velocity profile was specified as a parallel flow with a parabolic horizontal component given by $u(z) = 25z(0.5 - z)$ for $0 \leqslant z \leqslant 0.5$. As outflow boundary condition a parallel, fully developed flow was assumed for the components of the velocity vector and constant static pressure at the exit cross-sectional area was imposed. For this reason and for the present *Re* the total dimensionless length of the channel was taken equal to 30.

Profiles of both velocity components *u* and *w* and comparisons with the corresponding numerical results from Reference 23 are presented in Figures 7(a) and 7(b). The two developed recirculation zones that are formed are clearly depicted by the representation of the streamfunction contours in Figure 8.

The exact determination of the extent of the recirculation zones is achieved with the calculation of the shear stress distributions along the upper and lower walls, which are shown in Figure 9. In this figure the calculated stress distributions are also compared with the corresponding results from Reference 23 with noticeable agreement. The precise locations of separation and reattachment points
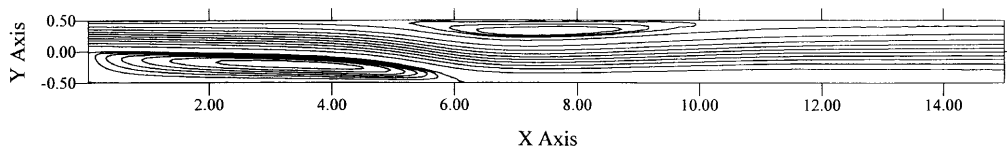

Figure 8. Streamfunction contours for clear representation of two recirculation zones· The formatted level values are -0.30, -0.025, -0.020, -0.015, -0.010, -0.005, 0.0, 0.050, 0.100, 0.150, 0.200, 0.250, 0.300, 0.350, 0.400, 0.450, 0.490, 0.500, 0.502 and 0.504
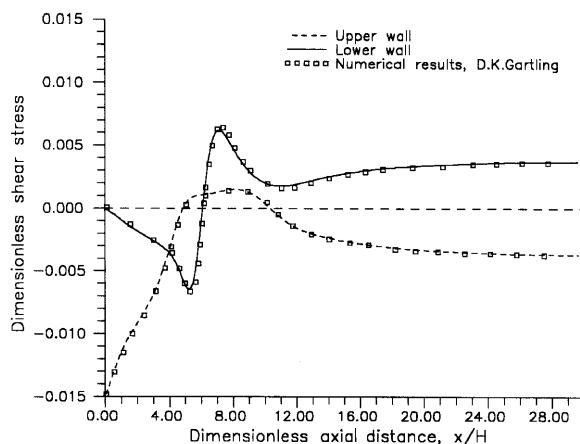

Figure 9. Shear stress distributions along upper and lower channel walls

Table I. Comparison of derived recirculation regions with corresponding results of a finite element method[23]

	Lower wall eddy	Upper wall eddy		
	Length of recirculation zone	Separation point	Reattachment point	Length of recirculation zone
FVS method (grid 150 × 31)	6.10	4.87	10.37	5.50
Gartling[23] (grids 400 × 20, 600 × 30, 800 × 40)	6.10	4.85	10.48	5.63

for the present numerical method as compared with the corresponding ones from the literature are presented in Table I.

Also important for the validation of the present results is the precise prediction of the pressure level inside the resultant flow field. By using as reference pressure the pressure on the edge of the backward-facing step, comparisons of the pressure profiles at cross-sections $x = 7$ and 15 with the corresponding ones from the literature are shown in Figure 10. Furthermore, comparisons of the pressure distributions along the upper and lower walls are presented in Figures 11(a) and 11(b).

It is reasonable to conclude from the above comparisons that the behaviour of the flow field predicted by the present numerical method (with the use of quite a coarse grid, 150 × 31) is in excellent agreement with the corresponding data from the literature obtained by other numerical methods.

The grid used for the solution of the flow field is the 150 × 31 non-uniform grid (coarser in the vicinity of the facing step) shown in Figure 6(b). The grid independence of the above results was examined with the use of a 200 × 41 uniform grid. The results were identical for the two grids; as an indication of this fact the velocity profiles of Figures 12(a) and 12(b) are presented.

4.1.3. Flow over a backward-facing step for various Re. In this case of flow over a backward-facing step the segment from the inlet of the channel to the expansion of the channel was taken into account for the calculation of the flow field. Thus the computational grid that was used for the discrete representation of the flow domain is non-Cartesian.
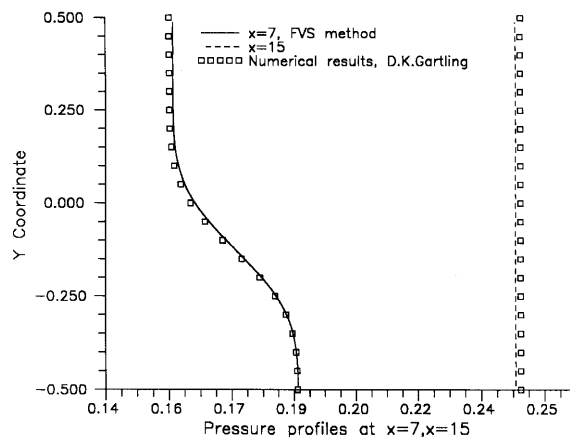
Figure 10. Pressure profiles across channel at cross-sections $x = 7$ and 15
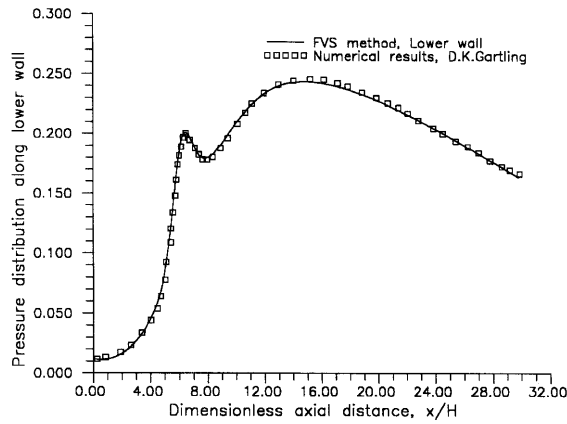
(a)
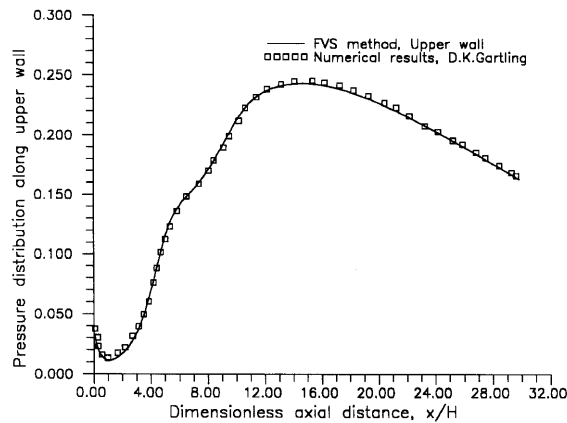
(b)

Figure 11. Pressure distributions along (a) lower and (b) upper channel walls

The geometrical data and the computational grid (200×25) are shown in Figure 13. The ratio of the expanded channel height (H) to the inlet height ($2h$) is two. The reference quantities that were used for the calculation of Re are the mean velocity of the fluid at the inlet as U_{ref} and the half-height of the inlet channel (h) as L_{ref}. The total dimensionless length of the channel was taken as $L = 50$.

The flow field over this backward-facing step was calculated for 10 different Reynolds numbers (in the range 7–115) in order to predict the recirculation length downstream of the sudden expansion of the channel. The resultant lengths were compared with the corresponding experimental data from the literature.[22,23] For the above range of Re, linear relationships between the recirculation length and Re are concluded in the literature. Sobey[24] gives $L_s = 2 + 0.13\, Re$ and Armaly et al.[22] give $L_s = 2 + 0.14\, Re$ (Figure 14).

4.2. Flow in a square cavity

This case of flow is usually examined for testing and evaluating numerical techniques because of the simplicity of the geometry and the complexity of the developed flow field with multiple regions
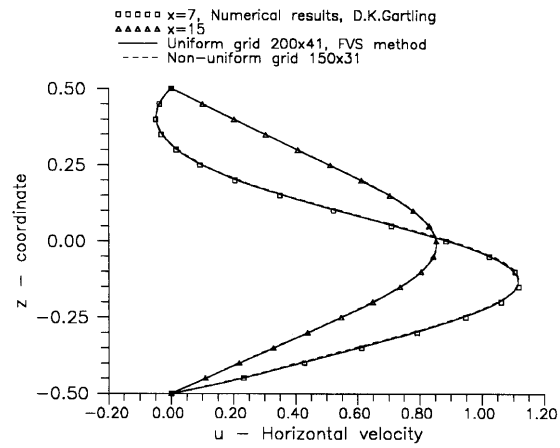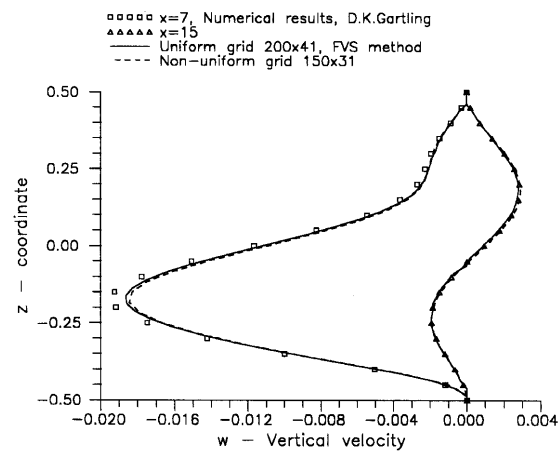
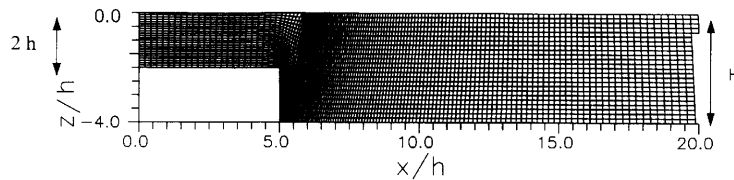Figure 12. (a) Horizontal and (b) vertical velocity profiles at sections $x = 7$ and 15 for two different grids

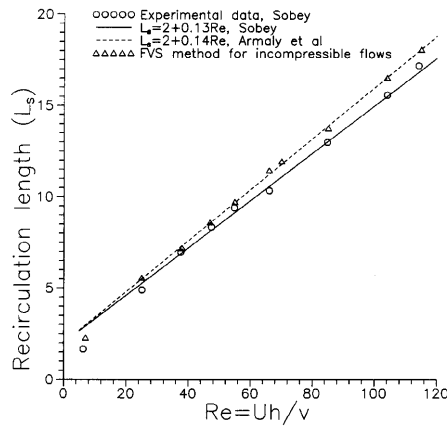Figure 13. Numerical grid (200×25) for representation of flow field over backward-facing step

Figure 14. Recirculation lengths for various *Re* and comparison with experimental data from literature

of recirculation near the corners. The geometry of the computational domain is shown in Figure 15. The quantities that were used for the calculation of the Reynolds number were the lid speed as U_{ref} and the length of the side of the square cavity as L_{ref}. Thus the dimensionless *u*-velocity profile at the top boundary was set at $u = 1$ and on the other boundaries the no-slip condition was applied.

Here the flow problem in a cavity was solved for three Reynolds numbers (100, 400 and 3200) and for various grid refinements. The presented profiles concern the *u*-velocity component on the vertical centreline of the cavity ($x = 0.5$), the *w*-velocity component along the horizontal centreline of the cavity ($z = 0.5$) (Figures 16(a)–16(f)) and their comparisons with the corresponding numerical[25,26] and experimental[27] data from the literature. The dimensions of the uniform grids that have been used for the flow field with $Re = 100$, 400 and 3200 are 40 × 40, 80 × 80 and 120 × 120 respectively. For the above Reynolds numbers the grid independence of the resultant flow fields has been examined with the use of 80 × 80, 100 × 100 and 140 × 140 uniform grids respectively.

The streamline and vorticity contours for the cavity flow configurations with *Re* increasing from 100 to 3200 are shown in Figures 17(a)–17(f) in order to give a clear impression of the flow field. As is well known and clearly seen in these figures, the centre of the primary vortex is offset towards the top right corner at $Re = 100$ and moves towards the geometrical centre of the cavity with an increase in *Re*. The extent and position of all the secondary vortices that are developed near the corners of the
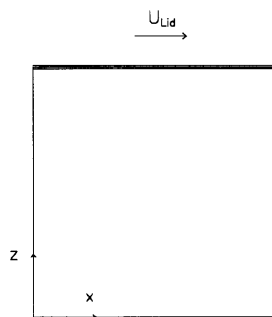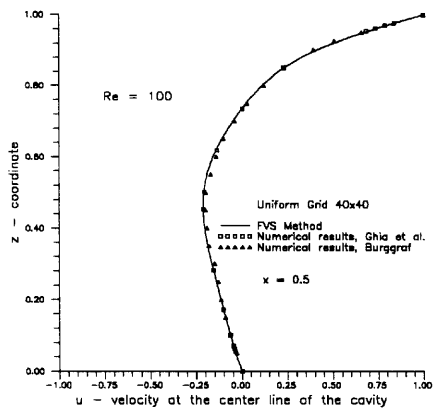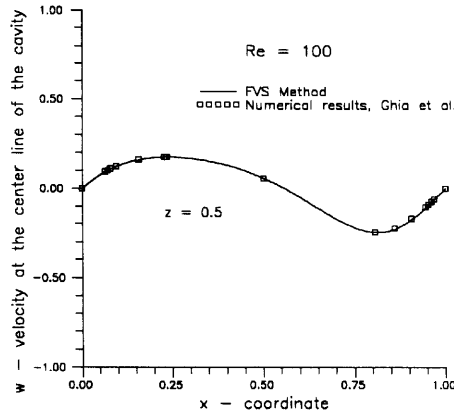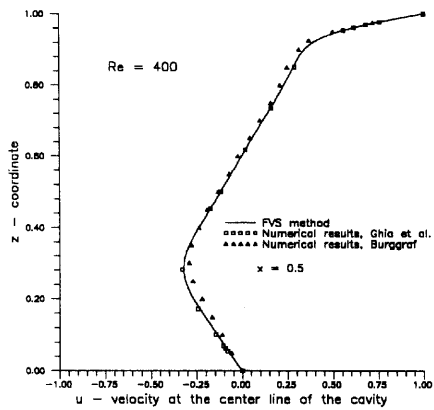

Figure 15. Schematic representation of cavity geometry

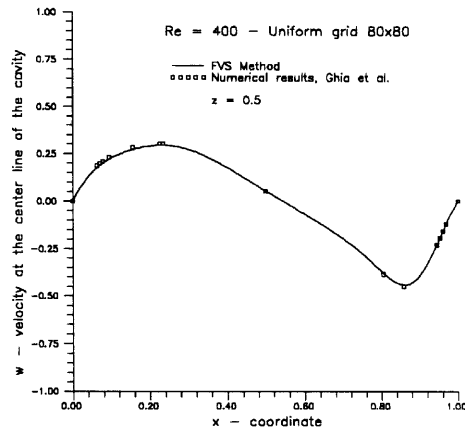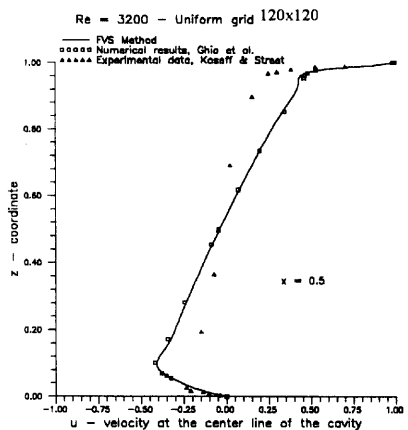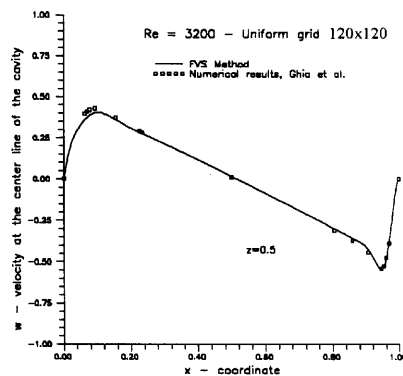Figure 16. Comparisons of u- and w-velocity profiles at centrelines of cavity:[24] (a), (b) $Re = 100$; (c), (d) $Re = 400$; (e),
(f) $Re = 3200$

Re=100, uniform grid 40x40
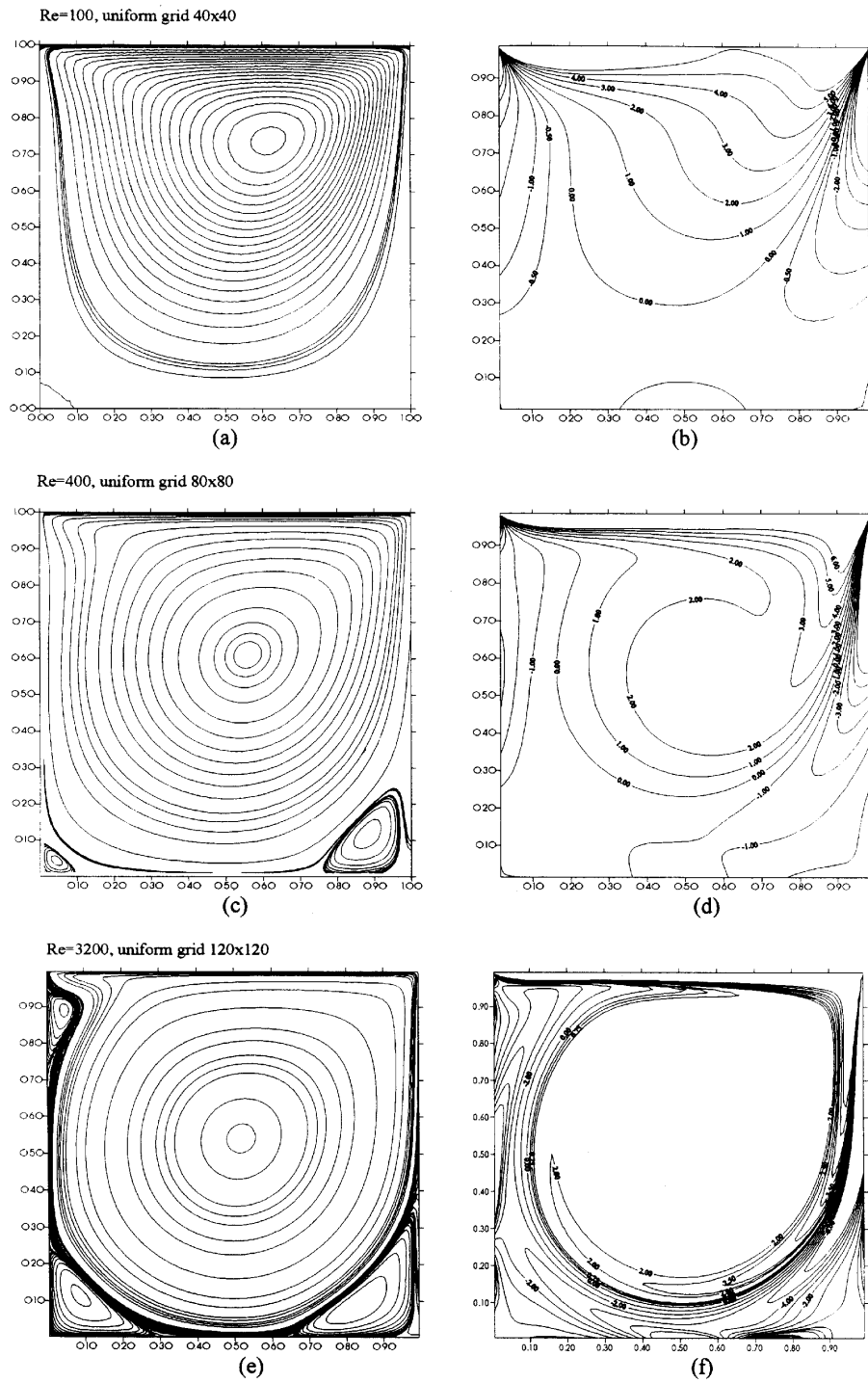
Re=400, uniform grid 80x80

Re=3200, uniform grid 120x120

Figure 17. Streamline and vorticity contours for cavity flow: (a), (b) $Re = 100$; (c), (d) $Re = 400$; (e), (f) $Re = 3200$

cavity are in excellent agreement with other numerical methods from the literature.[25] Similar agreement is observed for the contours of the vorticity function. As Re increases, several regions of high vorticity gradient, indicated by concentration of the vorticity contours, appear within the cavity.

The convergence histories of the flow field primitive variables for $Re = 100$ and 400 are shown in Figures 18(a) and 18(b). The convergence criterion used is that the maximum residual of the primitive flow variables in the entire flow field must be less than 1×10^{-5}. In most cases a sufficient limit for convergence to a steady state is 1×10^{-4}. The abrupt reduction of the pressure residual is
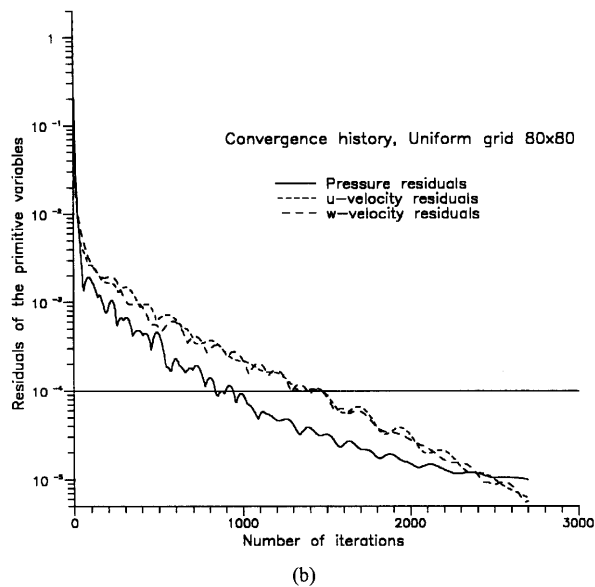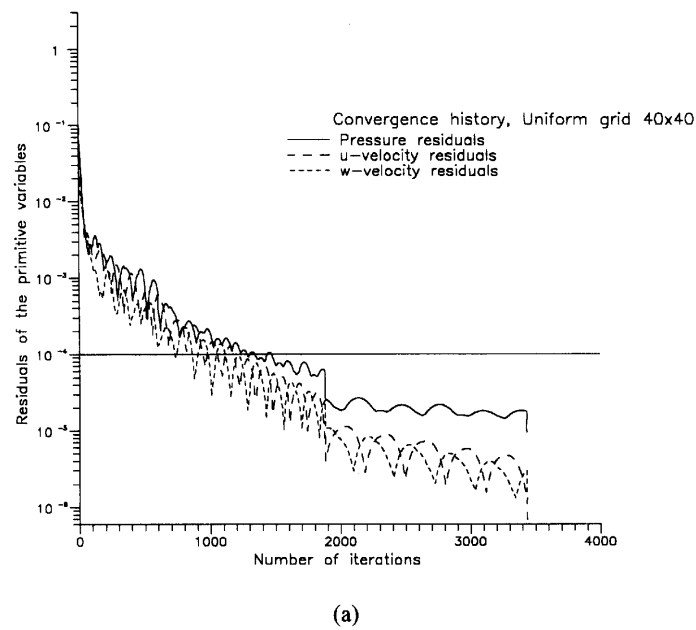

(a)

(b)

Figure 18. Convergence histories of flow field primitive variables: (a) $Re = 100$; (b) $Re = 400$

due to the external reduction of the corresponding underrelaxation factor for the acceleration of convergence in cases where it is slower (low *Re*).

4.3. Comments on present FVS method

In this subsection some general observations on the behaviour of the above-described method are presented.

Of upwind schemes used for most cases examined, those of third-order accuracy give solutions with better precision according to the density of the numerical grid. Of the third-order-accurate upwind schemes, the MUSCL scheme with limiters appears to have a better behaviour regarding the convergence history of the flow field variables, i.e. the number of iterations until convergence is achieved and the rate of reduction of the pressure residual as the flow field reaches a steady state. The last remark is mentioned because of the FVS method, as for most numerical methods for incompressible flow fields, the pressure converges to the desired rate with more difficulty than the velocity components do, and additionally, for pseudocompressibility methods, the pressure residuals represent the order of convergence of the continuity equation. The above remarks for the upwind schemes are described in Figure 19 for the flow over a backward-facing step. An additional concept illustrated in this figure, which could be investigated extensively, is that of thin layer approximation for the viscous terms, when a streamwise direction exists for the examined flow field, in order to reduce the computational time.

One of the characteristic properties of the upwind schemes is the ability to transmit 'information' on the field in accordance with the direction of transmission which is indicated by the characteristic curves of the field. The upwind representations are therefore more sensitive to the construction of the grid used for the discretization of the computational domain. In order to establish this fact, an 80×80 non-uniform grid (Figure 20(a)) that is finer near the solid boundaries, where the development of the boundary layer occurs, is used for the prediction of the flow field for $Re = 3200$. The computational results for the velocity profiles at the centrelines of the cavity are shown in Figure 20(b) in comparison with the corresponding results derived with a 120×120 uniform grid (these results have been tested in Section 4.2). The accuracy of the computational results for this difficult case of flow is evident.
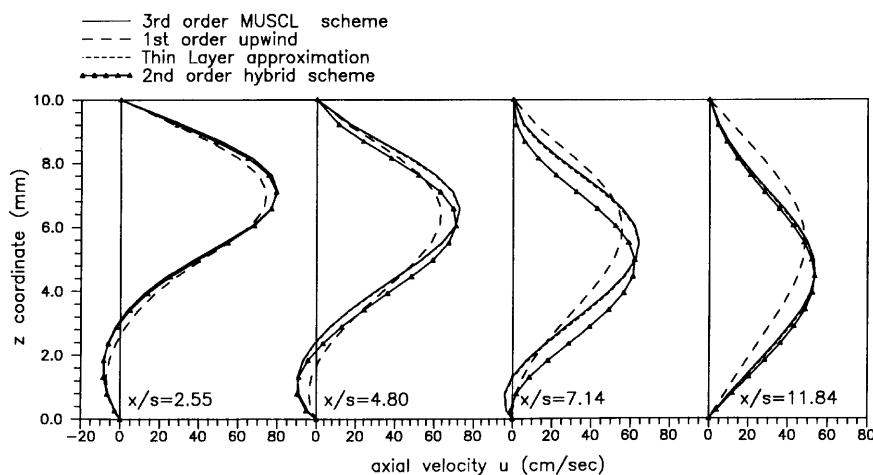

Figure 19. Plots of *u*-velocity component at four stations for flow over backward-facing step using various upwind schemes and thin layer approximation
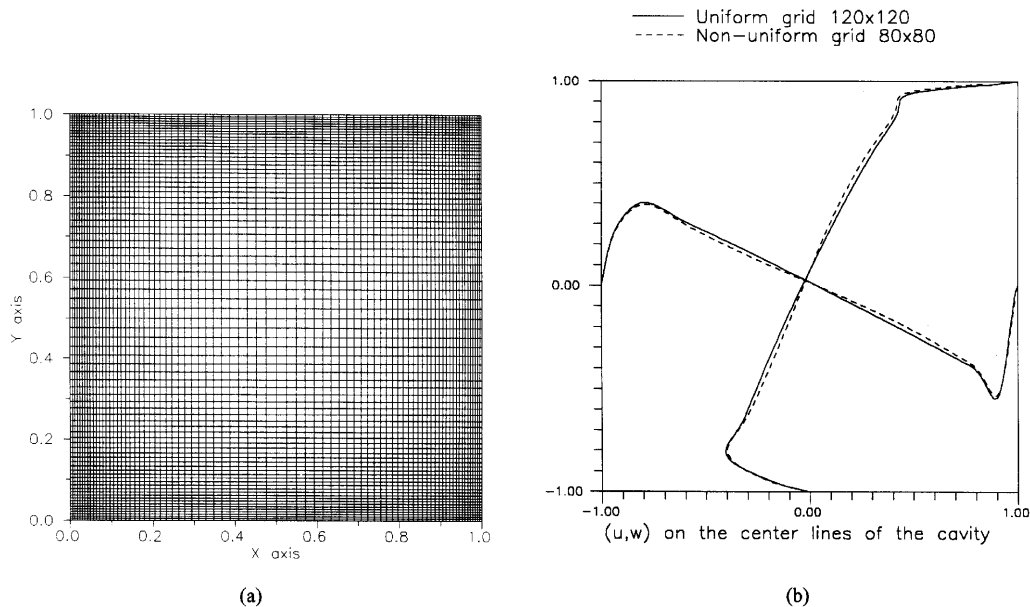
Figure 20 (a) Non-uniform 80 × 80 numerical grid for cavity. (b) Plots of *u*- and *w*-velocity components at centrelines of cavity for two different grids

5. CONCLUSIONS

The object of the present work was to develop an efficient numerical method for the solution of incompressible flow fields, based on the hyperbolic character of the Navier–Stokes equations when a pseudocompressibility term is added to the continuity equation. It is about the FVS method, which is a well known shock-capturing method for the solution of compressible flows. For incompressible flows the FVS method with the use of upwind schemes transmits 'information' inside the flow field in accordance with the sign of the eigenvalues of the resultant hyperbolic system of governing equations. A very important element of the developed method is that the unfactored discretized Navier–Stokes equations are solved by an implicit first-order-accurate (in time) scheme using a Gauss–Seidel relaxation technique. The unfactored scheme alleviates errors that coexist with an implicit method of approximate factorization. Furthermore, the use of upwind schemes makes the coefficient matrices diagonally dominant and allows, in relation to the unfactored scheme, the use of high CFL numbers (up to 10,000), consequently accelerating the convergence of the examined flow fields. In this work we also examined various upwind schemes used for the discrete representation of the flow field variables at cell faces, their influence on the accuracy of the method and the convergence history until a steady state is reached.

The formulation of the present FVS method was examined and validated for different flow cases, comparing them against experimental and numerical results from the literature with excellent agreement.

Extension of the present FVS method to unsteady flows is a subject of current research.

REFERENCES

1. H. Harlow and J. E. Walsh, 'Numerical calculation of time dependent viscous incompressible flow with free surface', *Phys. Fluids*, **8**, 2182–2189 (1965).

2. J. Chorin, 'A numerical method for solving incompressible viscous problems', *J. Comput. Phys.*, **2**, 12–26 (1967).
3. L. Steger and P. Kutler, 'Implicit finite-difference procedures for the computation of vortex wakes', *AIAA J.*, **15**, 581–590 (1977).
4. R. Peyret and T. D. Taylor, *Computational Methods for Fluid Flow*, Springer, New York, 1983.
5. J. L. C. Chang and D. Kwak, 'On the method of pseudocompressibility for numerically solving incompressible flows', *AIAA Paper 84-252*, 1984.
6. D. Choi and C. L. Merkle, 'Application of time-iterative schemes to incompressible flow', *AIAA J.*, **23**, 1519–1524 (1985).
7. A. Rizzi and L. Erikson, 'Computation of inviscid incompressible flow with rotation', *J. Fluid Mech.*, **153**, 275–312 (1985).
8. D. Kwak, J. L. C. Chang, S. P. Shanks and S. R. Chakravarthy, 'A three dimensional incompressible flow solving using primitive variables', *AIAA J.*, **24**, 390–396 (1986).
9. C. Merkle and M. A. Athavale, 'Time accurate unsteady incompressible flow algorithms based on artificial compressibility', *AIAA Paper 87–1137*, 1987.
10. W. Y. Soh and J. W. Goodrich, 'Unsteady solution of incompressible Navier–Stokes equations', *J. Comput. Phys.*, **79**, 113–134 (1988).
11. L. Thomas and R. W. Walters, 'Upwind relaxation algorithms for the Navier–Stokes equations', *AIAA Paper 85-1501-CP*, 1985.
12. M. Hartwich, C. H. Hsu and C. H. Liu, 'Vectorizable implicit algorithms for the flux-difference split, three-dimensional Navier–Stokes equations', *J. Fluids Eng.*, **110**, 297–305 (1988).
13. S. E. Rogers and D. Kwak, 'Upwind differencing scheme for the time accurate incompressible Navier–Stokes equations', *AIAA J.*, **28**, 253–262 (1990).
14. R. M. Beam and R. F. Warming, 'An implicit finite-difference algorithm for hyperbolic system of conservation-law form', *J. Comput. Phys.*, **22**, 87–110 (1976).
15. J. L. Steger and R. F. Warming, 'Flux vector splitting of the inviscid gasdynamics equations with application to finite difference methods', *J. Comput. Phys.*, **40**, 263–293 (1981).
16. B. van Leer, 'Flux vector splitting for the Euler equations', *Lecture Notes in Physics*, Vol. 170, Springer, Berlin, 1982, pp. 507–512.
17. D. Drikakis, 'Development of upwind numerical methods in high speed aerodynamics', *Ph.D. Thesis*, National Technical University of Athens, 1993.
18. D. Drikakis and S. Tsangaris, 'An implicit characteristics flux averaging scheme for the Euler equations for real gases', *Int. j. numer. methods fluids*, **12**, 771–776 (1991).
19. D. Drikakis and S. Tsangaris, 'On the solution of the compressible Navier–Stokes equations, using improved flux vector splitting methods', *Appl. Math. Model.*, **17**, 282–297 (1993).
20. M. A. Schmatz, 'Three dimensional viscous flow simulation using an implicit relaxation scheme', *MBB-LKE122-S-PUB-309*, 1987.
21. G. D. van Albada, B. van Leer and W. W., Roberts, 'A comparative study of computational methods in cosmic gasdynamics', *Astron. Astrophys.*, **108**, 76–84 (1982).
22. B. F. Armaly, F. Durst, J. Pereira and B. Schonung, 'Experimental and theoretical investigation of backward-facing step flow', *J. Fluid Mech.*, **127**, 473–496 (1983).
23. D. K. Gartling, 'A test problem for outflow boundary condition—flow over a backward facing step', *Int. j. numer. methods fluids*, **11**, 953–967 (1990).
24. I. J. Sobey, 'Observation of waves during oscillatory channel flow', *J. Fluid Mech.*, **151**, 395–426 (1985).
25. U. Ghia, K. N. Ghia and C. T. Shin, 'High-*Re* solutions for incompressible flow using the Navier–Stokes equations and a multigrid method', *J. Comput. Phys.*, **48**, 387–411 (1981).
26. O. R. Burggraf, 'Analytical and numerical studies of the structure of steady separated flows', *J. Fluid Mech.*, **24**, 113 (1966).
27. J. R. Koseff and R. L. Street, 'The lid-driven cavity flow: a synthesis of qualitative and quantitative observations', *J. Fluids Eng.*, **106**, 390–398 (1984).